Geopotential Field Anomaly Continuation with Multi-Altitude Observations

Jeong Woo Kim[1], Hyung Rae Kim[2], Ralph von Frese[3], Patrick Taylor[4], Elena Rangelova[1]

[1] Dept. of Geomatics Engineering, The University of Calgary, Calgary, AB T2N1N4, CANADA

[2] Dept. of Geoenvironmental Sciences, Kongju National University, Kongju, 314-701, KOREA

[3] School of Earth Sciences, The Ohio State University, Columbus, OH 43210, USA

[4] Goddard Space Flight Center, National Aeronautics and Space Administration, Greenbelt, MD 20771, USA

ABSTRACT

Conventional gravity and magnetic anomaly continuation invokes the standard Poisson boundary condition of a zero anomaly at an infinite vertical distance from the observation surface. This simple continuation is limited, however, where multiple altitude slices of the anomaly field have been observed. Increasingly, areas are becoming available constrained by multiple boundary conditions from surface, airborne, and satellite surveys. This paper describes the implementation of continuation with multi-altitude boundary conditions in Cartesian and spherical coordinates and investigates the advantages and limitations of these applications. Continuations by EPS (Equivalent Point Source) inversion and the FT (Fourier Transform), as well as by SCHA (Spherical Cap Harmonic Analysis) are considered. These methods were selected because they are especially well suited for analyzing multi-altitude data over finite patches of the earth such as covered by the ADMAP database. In general, continuations constrained by multi-altitude data surfaces are invariably superior to those constrained by a single altitude data surface due to anomaly measurement errors and the non-uniqueness of continuation.

Key words: Anomaly continuation, equivalent point source inversion, Fourier transform, spherical cap harmonic analysis

I. INTRODUCTION

In practice, no gravity or magnetic observation can be made with infinite accuracy. Thus, the further apart the truncated observations are from each other, the more biased they will be to different spatial attributes of the sources. This result makes it extremely problematic to relate, for example, truncated satellite altitude anomaly observations over hundreds of kilometers to imperfectly measured observations at the earth's surface by simple downward continuation of the satellite data or upward continuation of the near-surface data (e.g., Schnetzer, 1985; Grauch, 1993; von Frese et al., 1999; 2005; Ravat et al., 2002; Kim et al., 2004; 2005). Measurement errors alone restrict the utility of spaceborne anomaly continuations typically to within approximately ±50 km of mission altitude (von Frese et al., 2005). The problematic attributes of downward continuation, in particular, require that analyses of spaceborne geopotential observations be conducted essentially at satellite altitudes, unless they are integrated into a model that is also constrained by lower altitude observations.

Measurement errors also result in uncertainties in the spectral properties of the anomaly observations that grow with increasing difference in the survey altitudes. **Figure 1**, for example, compares the spectral properties of North American crustal magnetic anomalies mapped by typical satellite surveys at 400 km (e.g., Magsat and CHAMP) and the Decade of North American Geology (DNAG) compilation of aeromagnetic survey data (Hildenbrand et al., 1996). The comparison reveals a significant spectral gap between the two data sets with wavelengths comparable in scale to the magnetic effects of major crustal features. Due to measurement errors and the fundamental non-uniqueness of potential field continuation, there ultimately is no substitute to actual surveying for recovering these intermediate wavelength anomalies. Here, the intermediate wavelength anomalies might be substantially recovered by additional surveying at 20 km altitude with U2 surveillance or other high-altitude aircraft (Hildenbrand et al., 1996).

Global spherical harmonic models of the Earth's gravity (*e.g.*, Lemoine et al., 1998) and magnetic (Maus et al., 2009) fields are becoming increasingly available which are constrained by both satellite altitude and near-surface (i.e., terrestrial, marine and airborne) measurements. However, in contrast to the nearly global coverage that the satellite surveys provide, the coverage from near-surface surveys is far from global. Thus, when implementing near-surface predictions

60 from these models, particular care must be taken to verify that the predictions are constrained by
61 actual survey data.

62 Most geological gravity and magnetic anomaly studies tend to invoke local patches of
63 coverage and complementary subsurface geological and geophysical constraints that are difficult
64 to accommodate at the global scale of spherical harmonic modeling (*e.g.*, von Frese and Kim,
65 2003). Alternate approaches that are well suited for local applications in Cartesian and spherical
66 coordinates include equivalent point source (EPS) inversion, the Fourier transform (FT) in
67 Cartesian coordinates, and spherical cap harmonic analysis (SCHA) in spherical coordinates.
68 These procedures are all applicable to gravity and magnetic studies of the Antarctic lithosphere
69 south of 60°S. The sections below describe their uses for continuing multi-altitude data and
70 consider the relative advantages and limitations of these applications.

71

72 **II. EQUIVALENT POINT SOURCE (EPS) CONTINUATION**

73 In this section, EPS inversion is investigated for modeling anomaly continuations based on
74 single- and dual-altitude boundary conditions and using satellite crustal anomalies to fill in the
75 gaps in the near-surface survey coverage of the ADMAP database. EPS inversion has a long
76 history of estimating interpolations, continuations, and other derivative and integral components
77 of anomaly observations (e.g., Dampney, 1969; Ku, 1977; Mayhew, 1982; von Frese et al., 1981;
78 1998; Asgharzadeh et al., 2007; 2008).

79 The EPS effect is the fundamental integrand for all forward modeling integrals in gravity and
80 magnetic analysis (e.g., Blakely, 1995). For typical crustal ADMAP applications, it is
81 convenient to express the gravity point pole and magnetic point dipole effects in terms of the
82 spherical prism. More specifically, the gravity effect of the crustal prism in spherical (r, θ, φ)
83 coordinates with uniform density (= mass/unit volume) contrast $\Delta\sigma$ (e.g., von Frese et al., 1981;
84 Asgharzadeh et al., 2007) is

$$\Delta g(r,\theta,\varphi) \approx \Delta\varphi'_l \sum_{l=1}^{nl}\{\Delta\theta'_j \sum_{j=1}^{nj}(\Delta r'_i \sum_{i=1}^{ni}[-G\frac{\partial}{\partial R}(\frac{1}{R})\frac{\partial R}{\partial r}\Delta\sigma]A_i r_i^2)A_j \sin\theta_j\}A_l \ , \tag{1}$$

3

86   where G is the universal gravitational constant, R is the displacement between the source and

87   observation points with respectively primed and unprimed coordinates, and (A_i, A_j, A_l) are the

88   Gaussian-Legendre quadrature coefficients for the (nl×nj×ni) point sources used to approximate

89   the prism's volume (e.g., Stroud and Secrest, 1966). In addition,

90
$$\Delta\varphi'_l = [(\varphi'_{la} - \varphi'_{lb})/2], \Delta\theta'_j = [(\theta'_{ja} - \theta'_{jb})/2], \Delta r'_i = [(r'_{ia} - r'_{ib})/2] , \qquad (2)$$

91   where $(\varphi'_{la}, \varphi'_{lb})$, $(\theta'_{ja}, \theta'_{jb})$, and (r'_{ia}, r'_{ib}) are the lower (a) and upper (b) boundaries of the prism

92   in the l-th coordinate of longitude (φ), the j-th coordinate of co-latitude (θ), and i-th radial

93   coordinate (r). For completeness, note that Ku (1977) gives the equivalent Gauss-Legendre

94   quadrature (GLQ) gravity effect of the prism in Cartesian coordinates.

95   The total magnetic effect (ΔT) of the crustal prism, on the other hand, with uniform

96   magnetization (= dipole moment/unit volume) contrast Δm in spherical coordinates (e.g., von

97   Frese et al., 1981; 1998; Asgharzadeh et al., 2008) is

98
$$\Delta T(r, \theta, \varphi) \approx \Delta\varphi'_l \sum_{l=1}^{nl}\{\Delta\theta'_j \sum_{j=1}^{nj}(\Delta r'_i \sum_{i=1}^{ni}[\vec{u} \bullet \vec{\nabla}\{\vec{u}'\bullet\vec{\nabla}'(\frac{1}{R})\}\Delta m]A_i r_i^2)A_j \sin\theta_j\}A_l , \qquad (3)$$

99   where the unit vectors $\vec{u}'$ in source coordinates $(r', \theta' \varphi')$ and $\vec{u}$ in observation coordinates $(r, \theta,$

100     $\varphi)$ are dotted into the source and observation coordinate gradient operators $\vec{\nabla}'$ and $\vec{\nabla}$,

101   respectively. The magnetization contrast Δm represents the integrated effect of remanent and

102   induced components, where the latter is the prism's volume magnetic susceptibility times the

103   intensity of the applied magnetic field at the source point. Again for completeness, note that Ku

104   (1977) gives the equivalent magnetic effect of the prism by GLQ integration in Cartesian

105   coordinates.

106   Now, continuation, like any potential field analysis, can be generalized in matrix notation by

107
$$\mathbf{AX} = \mathbf{B}, \qquad (4)$$

108   where $\mathbf{B}$ is the (n×1) column matrix containing the n-anomaly observations, and $\mathbf{AX}$ is the

109   forward model involving the (n × m) known coefficients of the design matrix $\mathbf{A}$ and the (m×1)

110   column matrix containing the m-unknown coefficients of the solution matrix **X**. The objective

111   for continuation is to find the coefficients of **X** such that **AX** closely models **B** whereupon **AX**

112   may be used evaluate the attributes of **B** at other coordinates. Most typically, the least squares

113   solution is found by

114
$$X = [A^T A]^{-1} A^T B \tag{5}$$

115   so that the sum of the squared residuals between the observations and the forward model's

116   predictions is minimum (e.g., von Frese et al., 1988).

117   **Eq. 2** and **Eq. 3** provide the forward models for relating respective gravity and magnetic

118   anomalies to prism models that can be used for anomaly continuation. In particular, by

119   specifying the geometric attributes of the prism model, the inversion (**Eq. 4**) can be set up to

120   solve for the respective density and magnetization contrasts (**Eq. 5**) so that the modeled

121   predictions (**AX**) match the observations (**B**) in a least squares sense. To obtain the

122   coefficients of the design matrix **A**, the model is initialized by simply running it with the

123   physical property (i.e., $\Delta\sigma$ or Δm) set to unity.

124   In practice, however, errors in computing the **A**-coefficients due to the computer's limited

125   working precision and other uncertainties in the forward modeling may yield an unstable solution

126   **X** with large and erratic values that are useless for predicting anything other than the original

127   observations in **B**. To obtain a more stable and better performing solution, the system in **Eq. 3** is

128   commonly evaluated for the damped least squares solution

129
$$X = [A^T A + (EV) \times I]^{-1} A^T B , \tag{5}$$

130   where **I** is the identity matrix, and the scalar EV is variously called the damping factor,

131   Marquardt parameter, or error variance (e.g., von Frese et al., 1988). The damped least squares

132   approach requires choosing a value of EV that is just large enough to stabilize the solution for

133   meaningful objective predictions (e.g., anomaly continuation, interpolation, etc.), yet small

134   enough that the initial predictions provide an acceptable match to the observations **B**. For any set

135   of observations and forward model, an essentially optimal value of EV can be selected from

136   trade-off diagrams that contrast these two sets of model predictions for varying EV-values (e.g.,

137   von Frese et al., 1988).

138   Adapting the above results for anomaly continuation constrained by one or more boundary

139   conditions is straightforward. Relating both airborne and satellite anomaly observations to a

140   crustal prism model, for example, involves constructing the design matrix $\mathbf{A} = [\mathbf{A}_{airborne} \; \mathbf{A}_{satellite}]^T$

141   for the observation vector $\mathbf{B} = [\mathbf{B}_{airborne} \; \mathbf{B}_{satellite}]^T$, where the submatrices $\mathbf{A}_{airborne}$ and $\mathbf{A}_{satellite}$

142   reflect the geometric relationships between the crustal prism source coordinates and the

143   coordinates of the airborne and satellite observations in the respective $\mathbf{B}_{airborne}$ and $\mathbf{B}_{satellite}$

144   subvectors.

145   To test the performance of single- *versus* multi-altitude boundary conditions in anomaly

146   continuation, **Eq. 2** and **Eq. 3** were used to model the respective gravity and magnetic effects of

147   the five crustal prisms (**Figure 2**) outlined in top left anomaly maps of **Figure 3** and **Figure 4**,

148   respectively. The prisms were modeled for density contrasts ranging between -1.2 g/cm^3 and 1.8

149   g/cm^3, and cgs-magnetic susceptibility of contrasts of 0.0061468 and -0.028831 relative to the

150   surrounding crustal rocks. All prisms were 25 km thick with tops at 5 km below sea level and

151   located in Balkan region between $34°$ - $43°$ N and $21°$- $30°$ W. the panel A of maps in **Figure 3**

152   shows the modeled gravity effects to the nearest mGal over a 35×35 grid spanning the study area

153   at altitudes of 5 km (top), 10 km, 100 km, 200 km, 400 km, and 600 km (bottom). Panel A of

154   **Figure 4** gives the complementary differentially reduced-to-pole (DRTP) magnetic effects to the

155   nearest nT (e.g., von Frese et al., 1981). The DRTP effects were obtained from **Eq. 3** assuming

156   vertical inclination of the applied field at all source and observation points with the field

157   intensities at all source points taken from the World Magnetic Model (WMM) 2005 (NOAA,

158   2005).

159   The continuation analysis focused on relating the simulated airborne and satellite altitude

160   effects at 10 km and 400 km above sea level, respectively, to 50×50 arrays of crustal point

161   masses and magnetic dipoles at depths of 40 km and 20 km, respectively, below sea level. These

162   EPS inversions used the simpler forward model given by the integrands within the square

163   brackets of **Eq. 2** and **Eq. 3** to obtain the relevant point mass (= $\Delta\sigma$ × unit volume) and dipole

164   moment (= Δm×unit volume) solutions, respectively. In the two figures, the **B-panels** show the

165   predictions from the EPS solutions constrained by the anomalies modeled at both 10 km and 400

166   km above sea level, whereas the **C-** and **D-panels** give the continuations derived only from the

167   single-surface effects at the respective 10 km and 400 km altitudes. Comparison of the dual-

168 surface continuations in the **B-panels** with the equivalent single-surface estimates in the **C-** and

169 **D-panels** amply demonstrates the advantages of multi-altitude constrained continuation models

170 especially for downward continuation.

171 The comparisons at 5 km, and 10 km through 600 km altitudes at 10 km intervals are detailed

172 further in **Figure 5**. The respective left and right panels demonstrate the performances of the

173 gravity and magnetic continuations in terms of their correlation coefficients and root-mean-

174 squared (RMS) differences with the effects of the five prisms. These results, of course, like those

175 from any potential field analysis, are not unique. However, they clearly demonstrate the

176 limitations of downward continuing satellite-only potential field observations. They also suggest

177 that the multi-altitude magnetic continuations could be improved by incorporating additional data

178 from around 60 km to 80 km altitudes.

179 EPS models constrained by satellite and near-surface magnetic data are effective for filling in

180 regional gaps in the near-surface survey coverage in the ADMAP compilation, which are

181 particularly extensive in East Antarctica. The first compilation used satellite magnetic

182 observations from the 400-km altitude, 6-month Magsat mission (Golynsky et al., 2001).

183 However, these satellite data were collected during austral summer and fall periods, and thus

184 maximally corrupted by external magnetic field variations. The Ørsted and CHAMP missions

185 obtained much cleaner Antarctic satellite magnetic observations from several austral winters at

186 altitudes of about 600 and 400 km, respectively, with measurement accuracies exceeding

187 Magsat's by roughly an order of magnitude. The initial Magsat-based predictions in the

188 ADMAP compilation have been replaced by Ørsted- and CHAMP-based gap predictions (von

189 Frese et al., 2008).

190 To obtain effective estimates of near-surface anomalies in the coverage gap, the inversion of

191 the satellite data was optimized to match the near-surface anomaly observations around the gap's

192 perimeter (Kim et al., 2004; 2007). **Figure 6** illustrates the relative utility of this approach for a

193 simulated regional gap in ADMAP's near-surface survey coverage of the West Antarctic

194 Peninsula and surrounding marine areas (Kim et al., 2004). **Map A** shows the original ADMAP

195 10-km grid at 5-km above sea level of marine and airborne survey data for the well covered

196 region. Due to the mission altitudes, the satellite data are mostly sensitive to the 400-km and

197　larger wavelength components of the near-surface data in **Map B**.　The low-pass filtered data
198　were related to a crustal prism model with negligible error that was evaluated at 400 km altitude
199　with an accuracy of 3 nT in **Map C** to simulate the effects of Magsat measurement errors.　The
200　crustal prism model was also evaluated to a 0.3 nT accuracy at altitudes of 400 km in **Map E** and
201　700 km in **Map G** to simulate the respective effects of CHAMP and Ørsted satellite observation
202　errors.

203　　　The simulated Magsat, CHAMP, and Ørsted data were combined with the near-surface data
204　around the white-outlined periphery of the simulated gap in **Map B** and related to crustal prism
205　models by least squares inversion.　The resultant prism models were then evaluated for the
206　respective Magsat-, CHAMP-, and Ørsted-based gap predictions shown in **Maps D, F,** and **H.**
207　**Table 1** compares the gap predictions against the original gap values from **Map B** in terms of the
208　RMS differences, correlation coefficients (CC) and noise levels from the noise (N)-to-(S) signal
209　ratio approximation (Foster and Guinzy, 1967) given by

$$\frac{N}{S} \approx \sqrt{\frac{1}{|CC|} - 1}\,. \tag{6}$$

211　The comparison also includes gap predictions from the application of minimum curvature (MC)
212　to the near-surface survey data.　In general, the simulated results suggest that the use of the
213　Ørsted and CHAMP data improves the gap estimates by nearly 75% relative to the Magsat-based
214　predictions.

215　　　An opportunity to test the multi-altitude gap prediction method resulted when a new
216　aeromagnetic survey was obtained in the regional gap located east of Coats Land and the
217　Shackleton Range as shown in **Map A** of **Figure 7** (Kim et al., 2007).　**Map B** gives the regional
218　200 km and longer wavelength components of the new survey data that are much more consistent
219　with the CHAMP- and Ørsted-based gap predictions in **Map C** than with the minimum curvature
220　estimates in **Map D** and the near-surface predictions of the spherical harmonic geomagnetic field
221　model MF4 (Maus and Rother, 2005) in **Map E.**

222　　　Of course, as for any inversion, the results of continuation are not unique. Thus, they do not
223　obviate the need for anomaly mapping in regions lacking measurements to better define the
224　geologic implications in existing anomaly observations.

8

225

III. FOURIER TRANSFORM (FT) CONTINUATION

227 Gravity and magnetic anomalies are mapped at elevations accessible by borehole, tunnel, ground

228 and ice surface, ocean and lake bottom, submarine, ship, airplane, balloon, space shuttle tether,

229 and satellite surveys. Where the horizontal dimensions of the survey are several hundred

230 kilometers or less, the data are commonly gridded at constant elevation and horizontal intervals

231 measured in linear units of length for analysis. In this case where the anomaly data are registered

232 to a Cartesian grid, effective anomaly continuation can be done most elegantly and efficiently

233 using the Fourier transform as the forward model of the inversion (e.g., Blakely, 1995).

234 The free-space behavior of gravity and magnetic anomalies S is governed by Laplace's

235 equation

236

$$(\frac{\partial^2}{\partial x^2} + \frac{\partial^2}{\partial y^2} + \frac{\partial^2}{\partial z^2})S = 0 \tag{7}$$

238 so that the vertical z-dimensional properties of the anomalies may be assessed from their mapped

239 x- and/or y-dimensional attributes. In particular, for gridded $S(x, y)$ with the gridded Fourier

240 transform $\overline{S}(l,k)$ in wavenumbers l and k, taking the Fourier transform of **Eq. 7** gives

241

$$\frac{\partial^2 \overline{S}}{\partial z^2} = (2\pi)^2 (f_l^2 + f_k^2)\overline{S} , \tag{8}$$

243 where $(f_l = l/M)$ and $(f_k = k/N)$ are the linear frequencies for the number of anomaly values M and

244 N in the x- and y-directions, respectively. **Eq. 8** is a second order differential equation with

245 constant coefficients that has the general solution

$$\overline{S}(z) = A \times e^{+z\sqrt{a}} + B \times e^{-z\sqrt{a}}, \tag{9}$$

247

248 where

$$a = 4\pi^2 (f_l^2 + f_k^2) . \tag{10}$$

250 Boundary conditions are commonly invoked to specify the form of the solution in **Eq. 9** that

251 is appropriate for application. By the classical Poisson boundary condition, acceptable solutions

252 are those that approach zero as the elevation z becomes infinite. Thus, for upward continuation

253 where $z > 0$, the boundary condition requires $A = 0$ so that the solution becomes

$$\bar{S}(z)_{upcon} = B \times e^{-z\sqrt{a}} . \tag{11}$$

255 Referencing the grid to $z = 0$ shows that $B = \bar{S}(0) \equiv \bar{S}$ so that the upward continuation of

256 the anomaly grid to any positive $z > 0$ is

$$\bar{S}(z)_{upcon} = \bar{S} \times e^{-z\sqrt{a}} . \tag{12}$$

258 Similarly, for downward continuation where $z < 0$, the boundary condition requires $B = 0$ so

259 that the solution is

260

$$\bar{S}(z)_{dwcon} = A \times e^{+z\sqrt{a}} . \tag{13}$$

262 Again, taking the elevation of the grid as relative zero shows that $A = \bar{S}(0) \equiv \bar{S}$ so that the

263 downward continuation of the anomaly grid to negative $z < 0$ is

$$\bar{S}(z)_{dwcon} = \bar{S} \times e^{+z\sqrt{a}} . \tag{14}$$

265 Inversely transforming **Eq. 12** and **Eq. 14** is the conventional approach for upward and

266 downward continuing a single anomaly grid through positive and negative elevations about its

267 elevation (e.g., Pawlowski, 1995; Fedi and Florio, 2002; Cooper, 2004). The singular uses of the

268 A and B coefficients in **Eq. 9** define the two end member solutions for downward and upward

269 continuation, respectively. However, multiple altitude anomaly grids are becoming increasingly

270 available where both coefficients may be applied to evaluate the anomaly values at the

271 intermediate altitudes between the grids.

272 Specifically, let the lower altitude anomaly grid be referenced to relative zero and the higher

273 altitude grid be referenced to an elevation H where the Fourier transforms of $S(0)$ and $S(H)$ are

274 $\bar{S}(0)$ and $\bar{S}(H)$, respectively. Both transforms may be related through **Eq. 9** to common A and

275 B coefficients given by

276

$$A = \frac{\bar{S}(0)e^{-z\sqrt{a}} - \bar{S}(H)}{e^{-z\sqrt{a}}} \quad \text{and} \quad B = \frac{\bar{S}(H) - \bar{S}(0)e^{+H\sqrt{a}}}{e^{-z\sqrt{a}}} \tag{13}$$

278

279   so that the continued field at an intermediate z-altitude for all $0 \le z \le H$ is

280

281    $$\bar{S}(z) = \frac{1}{t}\left[\bar{S}(0)e^{-H\sqrt{a}}e^{+z\sqrt{a}} - \bar{S}(H)e^{+z\sqrt{a}} + \bar{S}(H)e^{-z\sqrt{a}} - \bar{S}(0)e^{+H\sqrt{a}}e^{-z\sqrt{a}}\right]$$

282    $$= \frac{1}{t}\left[\bar{S}(0)(e^{+(z-H)\sqrt{a}} - e^{-(z-H)\sqrt{a}}) + \bar{S}(H)(e^{-z\sqrt{a}} - e^{+z\sqrt{a}})\right] \qquad (14)$$

283    $$= \frac{1}{t}\left[\begin{array}{c} e^{+(z-H)\sqrt{a}} - e^{-(z-H)\sqrt{a}} \\ e^{-z\sqrt{a}} - e^{+z\sqrt{a}} \end{array}\right]^{T}\left[\begin{array}{c} \bar{S}(0) \\ \bar{S}(H) \end{array}\right],$$

284

285   with

286    $$t = e^{-H\sqrt{a}} - e^{+H\sqrt{a}}. \qquad (15)$$

287

288   **Figure 8** illustrates the use of the dual Fourier transforms for two altitude slices of the noise-
289   free gravity effects for a simple model of two prisms. The gravity effects of the prisms were
290   calculated in Cartesian coordinates at relative 0 km (**Map A**) and at 16 km (**Map B**) and 20 km
291   (**Map C**) above the relative 0-km effects. **Map D** shows the dual altitude continuation estimates
292   at 16 km and **Map E** gives the difference between **Map B** and **Map D**. **Map F** is the
293   conventional downward continuation of **Map C** at 16 km, whereas **Map G** is the 16-km upward
294   continuation of **Map A** with **Map H** and **Map I** giving the related differences from the modeled
295   effects in **Map B**. The dual and single surface continuations are largely consistent, although the
296   dual surface estimates in **Map D** are clearly superior to the 4-km downward and 16-km upward
297   continued single surface estimates in **Maps F and G**.

298   The general consistency of the single- and dual-surface continuations in **Figure 8** is mostly
299   due to the source effects being minimally distorted in the two anomaly grids. This level of
300   source signal fidelity is not likely to occur in practice where, for example, in the lower altitude
301   grid the effects of near-surface sources mask within working precision elements of the more
302   regional source effects that in the higher altitude grid are preferentially expressed at the expense
303   of the shorter wavelength near-surface source effects. Measurement and anomaly reduction
304   errors also will substantively affect the fidelity of gridded source signals at the different altitudes.

305   As an example, **Figure 9** considers the altitude variations of the reduced-to-pole magnetic
306   anomalies over the southern Greenland area constrained by airborne (Verhoef et al., 1996) and
307   CHAMP satellite (Maus et al., 2002) measurements. The magnetic data were Fourier transformed
308   assuming the flat-earth approximation given the approximate 1,600 km by 1,600 km area of the
309   study (Strang van Hees, 1990). The single surface transform was used to upward continue the
310   airborne data to 20 km in **Map A**, 50 km in **Map B**, 250 km in **Map C**, 300 km in **Map D**, and
311   350 km in **Map E**. However, the CHAMP data at 350 km in **Map F** show a considerably
312   stronger effect over Iceland than is apparent in the upward continued airborne data of **Map E**.
313   Indeed, the dual surface FT continuations at 300 km in **Map G**, 250 km in **Map H**, and 50 km in
314   **Map I** suggest that this disparity persists at altitudes of 250 km and higher. Clearly, the CHAMP
315   data provide important additional constraints for developing a comprehensive crustal magnetic
316   model of the study area.
317
318   **IV. SPHERICAL CAP HARMONIC ANALYSIS (SCHA)**

319   Spaceborne and lower altitude magnetic and gravity anomalies obviously provide different
320   insights for resolving the crustal sources of the potential field anomalies. In particular, the lower
321   altitude anomalies provide much more detail on the crustal sources than can be observed at
322   satellite altitude. The satellite anomalies, on the other hand, typically yield better regional images
323   of the sources than can be obtained from regional compilations of the lower altitude anomalies
324   that have been mapped with disparate survey parameters. At regional scales of coverage such as
325   represented by the ADMAP compilation for the Antarctic area south of 60° S, the spherical cap
326   harmonic synthesis of satellite and near-surface potential field observations is particularly useful
327   and elegant model for crustal modeling. For example, it is analytically more useful than the
328   simple grid for representing the ADMAP compilation because it can directly estimate magnetic
329   anomalies and their gradient and tensor components anywhere on and above the Antarctic
330   surface (e.g., von Frese et al., 2008).

331   Spherical cap harmonic analysis (SCHA) was developed by Haines (1985) for geomagnetic
332   main and external magnetic field modeling at regional scales. It has also been extended to
333   regional magnetic studies of the lithosphere (e.g., Haines and Newitt, 1986; De Santis et al.,
334   1990; Kotzé, 2001; Thébault et al., 2006; Thébault and Gaya-Piqué, 2008; von Frese et al.,

335 2008), as well as gravity studies (e.g., Hwang and Chen, 2007; De Santis and Torta, 1997). This

336 approach adapts the global spherical harmonic solution to a spherical cap solution for the

337 magnetic potential

338

339
$$V(r,\theta,\varphi) = \sum_{n=0}^{N_{int}} \sum_{m=0}^{n} a \left(\frac{a}{r}\right)^{n+1} \left(g_n^{m,i} \cos m\varphi + h_n^{m,i} \sin m\varphi\right) P_n^m(\cos\theta) +$$

340
$$\sum_{n=1}^{N_{ext}} \sum_{m=0}^{n} a \left(\frac{a}{r}\right)^{n} \left(g_n^{m,e} \cos m\lambda\varphi + h_n^{m,e} \sin m\varphi\right) P_n^m(\cos\theta), \tag{16}$$

341

342 where N_{int} and N_{ext} are the maximum indices for internal and external sources, respectively, P_n^m

343 is a Legendre function of degree n and order m, and $g_n^{m,i}$, $h_n^{m,i}$, $g_n^{m,e}$, $h_n^{m,e}$ are the spherical

344 cap Gauss coefficients. If the half-angle of the spherical cap is denoted by ϑ_0, the $n_k(m)$ for a

345 given m are determined as the roots of

346

347
$$dP_n^m(\cos\theta_0)/d\theta = 0, k - m = \text{even}, \tag{17}$$

348

349 and additionally, where differentiability with respect to θ is required, of

350

351
$$dP_n^m(\cos\theta_0) = 0, k - m = \text{odd}. \tag{18}$$

352

353   Truncating the expansion in Equation (16) at $k = K$ sets the number of model coefficients at

354 $(K+1)^2$. When applying SCHA, a global spherical harmonic potential is typically removed from

355 the total potential to improve convergence as well as extrapolation beyond the spherical cap

356 boundary (Haines, 1985). In general, the maximum degree of a spherical cap harmonic model,

357 truncated at a certain number of model coefficients, is a function of the half-angle of the

358 spherical cap that determines the minimum wavelength resolution that can be obtained (e.g.,

359 Kotzé, 2001). As a radial distance is also included in the formulation, data over a range of

360 altitudes can be used to derive a model.

13

361   Two examples are presented in this study. The SCHA is a parametric method with the

362   coefficients of the harmonic representation of the gravity and magnetic potential being model's

363   parameters. This method has been proven to work with both gridded and irregularly distributed

364   data, which in example are along track data. We used a variation of the SCHA, in which the

365   spherical cap is mapped onto a hemisphere, thus ensuring the proper harmonic continuation of

366   the gravity and magnetic field anomalies and to different altitudes between satellite and the Earth

367   surface.

368

369   **Figure 10** shows the use of SCHA to model the effects of the NE Asia gravity field

370   developed by the Curtin University of Technology (CUT) in Western Australia (Kuhn and

371   Featherstone, 2005). The gravity anomalies were synthesized on a $1°$ x $1°$ grid with the center of

372   the spherical cap is $50°$ N and $130°$ E. In this example, the synthetic gravity anomaly data at the

373   Earth's surface (c) and 20 km altitude (a) were jointly modeled by the SCHA with negligible

374   error to obtain gravity anomalies at 10 km altitude (b) which show the compiled gravity

375   anomalies at 10 km altitude with a resolution of 200 km half-wavelength. The model errors

376   account for 10% of the gravity anomaly magnitude at most and can be further reduced by

377   increasing the spectral resolution of the model. Table 2 shows the statistics of synthetic gravity

378   data at 20, 10, and 0 km and correlation coefficients shown in **Figure 10**.

379

380   Another example modeling the radial geomagnetic field component at satellite (a), U2 (b)

381   altitudes and the Earth surface (c) is given in **Figure 11**. Here, the satellite altitude (685 km)

382   component for December 1999 was globally evaluated from the three-axis magnetometer

383   measurements of the KOrea Multi Purpose Satellite-1 (KOMPSAT-1) that provided the

384   satellite's attitude control (Kim et al., 2007) as shown **Figure 11** (a). These data were used to

385   estimate the radial components by the SCHA at satellite (685 km), U2 (20 km) altitudes and at

386   the Earth surface (0 km). Table 3 summarizes statistics and correlation coefficients of radial

387   component of KOMPSAT-1 measurements estimated at satellite (685 km), U2 (20 km), and

388   Earth surface (0 km) as shown in **Figure 11**. This example illustrates a further use of SCHA in

389   developing improved regional core field models for extracting crustal components in the survey

390   data.

391

14

392   The Antarctic Reference Model (ARM), for example, was developed for ADMAP

393   applications to best represent the spatial and temporal properties of the Antarctic core field as

394   recorded over the period 1960-2002 by an international network of 28 observatories and satellite

395   magnetic data from six missions (Gaya-Piqué et al., 2006). The SCHA predictions from ARM

396   have greater sensitivity for the Antarctic spatial and temporal variations of the core field than do

397   conventional global spherical harmonic geomagnetic field models like the IGRF-10 (IAGA,

398   2005).

399   Data from the Arctowski, Scott Base, Syowa, and Vostok geomagnetic observatory data

400   through 2003, for example, showed that the ARM estimates of the annual variations of the

401   Antarctic core field are roughly 31% and 22% better than the IGRF-10 and CM4 (Sabaka et al.,

402   2004) estimates, respectively. In addition, the core field predictions were checked at the Georg

403   von Neumayer observatory where data were obtained that had not been included in the original

404   ARM model. At this observatory, which was operated over the period 1983.5-1991.5 on the

405   coast of Dronning Maud Land ($70.617°$ S, $351.633°$ E), the ARM estimates were found to be 76%

406   and 75% better than the respective IGRF-10 and CM4 estimates. Additionally, ARM estimated

407   the mean secular variation some 78% and 75% better than the respective IGRF-9 and CM4

408   models.

409

410   **V. CONCLUSIONS**

411   Low-earth-orbiting satellites are recording state-of-the-art magnetic and gravity field

412   observations of the earth at altitudes ranging over roughly 300-700 km. However, the

413   measurement errors and non-uniqueness of the continuation process severely limit estimating

414   these anomalies at the near-surface. Indeed, numerical anomaly simulations from satellite to

415   airborne altitudes suggest that effective downward continuations of the satellite data are

416   restricted to within approximately 50 km of the observation altitudes while upward continuations

417   can be effective over a somewhat larger altitude range. Given current anomaly error levels, the

418   multi-altitude inversion of satellite and near-surface anomalies is a particularly promising

419   approach for implementing satellite geomagnetic observations for crustal studies.

420   This study investigated multi-altitude implementations of equivalent point source (EPS) and
421   spherical cap harmonic analysis (SCHA) modeling in spherical coordinates and the Fourier
422   transform (FT) for continuation in Cartesian coordinates. These implementations revealed that
423   the anomaly estimates at the intermediate altitudes from multi-altitude constrained models were
424   invariably superior to the classical downward and upward continuations of a single slice of the
425   anomaly field.   In addition, near-surface downward continuations of satellite altitude
426   observations or satellite altitude upward continuations of near-surface data can be severely
427   problematic due to measurement and data reduction errors and the inherent non-uniqueness of
428   any continuation. As a result, an observation's capacity to define a field's spatial behavior is
429   restricted in practice to a relatively small region about the observation site beyond which
430   mapping is required to confidently resolve the more distant spatial details of the field. In other
431   words, there ultimately is no substitute for mapping to establish the value of an anomaly field at
432   an unsurveyed location.

433

434   **VI. ACKNOWLEDGMENTS**

441

16

VII. REFERENCES

Asgharzadeh, M.F., R.R.B. von Frese, H.R. Kim, T.E. Leftwich, J.W. Kim, 2007, "Spherical prism gravity effects by Gauss-Legendre quadrature integration," Geophys. J. Int., v. 169, pp. 1-11.

Asgharzadeh, M.F., R.R.B. von Frese, H.R. Kim, 2008, "Spherical prism magnetic effects by Gauss-Legendre quadrature integration," Geophys. J. Int., v. 173, 315-333.

Blakely, R.J., 1995. Potential theory in gravity and magnetic applications, Cambridge University Press.

Cooper, G., 2004. The stable downward continuation of potential field data. Exploration Geophysics. 35, 260-265.

Dampney, C.N.G., 1969. The equivalent source technique. Geophysics. (45), 39-53.

De Santis A., Battelli, O., Kerridge, D.J., 1990. Spherical cap harmonic analysis applied to regional field modelling for Italy. J. Geomag. Geoelectr., 42, 1019-1036.

De Santis A., Torta, J.M., 1997. Spherical cap harmonic analysis: a comment on its proper use for local gravity field representation. J. Geodesy, 71, 526-532.

Fedi M., Florio G., 2002. A stable downward continuation by using the ISVD method. Geophysical J. Int., 151, 146-156.

Foster, M.R., Guinzy, N.J., 1967, The coefficient of coherence: its estimation and use in geophysical prospecting, Geophysics, 32, 602-616.

Gaya-Piqué, L.R., D. Ravat, A. de Santis, J.M. Torta, 2006. New model alternatives for improving the representation of the core magnetic field of Antarctica. Antarctic Sci. 18, 101-109.

Golynsky A., Chiappini, M. Damaske, D., Ferraccioli, F., Ferris, J., Finn, C., Ghidella, M., Isihara, T., Johnson, A., Kim, H.R., Kovacs, L., LaBrecque, J., Masolov, V., Nogi, Y., Purucker, M., Taylor, P., Torta, M., 2001. ADMAP - Magnetic Anomaly Map of the Antarctic, 1:10,000,000 scale map, in Morris P, and R von Frese, eds., BAS (Misc.) 10, Cambridge, British Antarctic Survey.

Grauch, V.J.S., 1993. Limitations on digital filtering of the DNAG magnetic data set for the conterminous US. Geophysics, 8, 1281-1296.

Hains, G.V., 1985. Spherical Cap Harmonic Analysis. J. Geophys. Res., 90(B3), 2583-2591.

17

472   Hains, G.V., Newitt, L.R., 1986. Canadian geomagnetic reference field. J. Geomag. Geoelectr.,
473   38, 895-921.

474   Hildenbrand, T.G., Blakely, R.J., Hinze, W.J., Keller, R., Langel, R.A., Nabighian, M., Roest
475   W.R., 1996. Aeromagnetic survey over US to advance geomagnetic research. EOS Trans.
476   Amer. Geophys. Un., 77, 265-268.

477   Hwang, C, Chen, S.K., 2007. Fully normalized spherical cap harmonics: application to the
478   analysis of sea-level data from TOPEX/POSEIDON and ERS-1. Geophysical. J. Int., 129,
479   450-460.

480   IAGA (International Association of Geomagnetism and Aeronomy), Division V, Working Group
481   V, 2005. The 10th generation international geomagnetic reference field. Geophys. J. Int., 161,
482   561–565.

483   Kim, H.R., von Frese, R.R.B., Golynsky, A.V., Taylor, P.T., Kim, J.W., 2004. Application of
484   satellite magnetic observations for estimating near-surface magnetic anomalies. Earth,
485   Planets, Space, 56, 955-966.

486   Kim, H.R., R.R.B. von Frese, Golynsky, A.V., P.T. Taylor, J.W. Kim, 2005, "Crustal
487   magnetization of Maud Rise in Antarctic and Southwest Indian Oceans, Earth, Planets, and
488   Space, v. 57, pp. 717-726.

489   Kim, H.R., Hwang, J.S., Suh, M.C., Kim, J.W., 2010. New approach in magnetic potential field
490   continuation by FFT. J. Econ. Environ. Geol. 43 (3), 249-258.

491   Kim, J.W., Hwang, J.S., von Frese, R.R.B., Kim, H.R., Lee, S.H., 2007. Geomagnetic field
492   modeling from satellite attitude control magnetometer measurements. J. Geophys. Res., 112,
493   B05105, doi:10.1029 /2005JB004042.

494   Kotzé, P.B., 2001. Spherical cap modelling of Ørsted magnetic field vectors over southern
495   Africa. Earth, Planets, Space, 53, 357-361.

496   Ku C.C., 1977. A direct computation of gravity and magnetic anomalies caused by 2- and 3-
497   dimensional bodies of arbitrary shape and arbitrary magnetic polarization by equivalent-point
498   method and a simplified cubic spline. Geophysics, 42, 610–622.

499   Kuhn, M., Featherstone, W.E., 2005. Construction of a synthetic Earth gravity model by forward
500   gravity modelling. In: Sanso F (ed) A Window on the Future of Geodesy. Springer, Berlin
501   Heidelberg New York, 350-355.

502   Lemoine et al., 1998. The Development of the Joint NASA GSFC and the National Imagery and
503   Mapping Agency (NIMA) Geopotential Model EGM96. NASA/TP-1998-206861.

504   Maus, S., Rother, M. Holme, R., Luehr, M., Olsen, N., Haak, V., 2002. First scalar magnetic
505   anomaly map from CHAMP satellite data indicates weak lithospheric field. Geophys. Res.
506   Lett., 29, 10.1029/2001GL013685.

507   Maus S., Rother, M., 2005. http://geomag.colorado.edu /litmod4.html.

508   Maus, S., U. Barckhausen, N. Bournas, J. Brozena, V. Childers, F. Dostaler, J.D. Fairhead, C.
509   Finn, R.R.B. von Frese, C. Gaina, S. Golynsky, R. Kucks, H. Lühr, P. Milligan, S. Mogren,
510   R.D. Müller, O. Olesen, M. Pilkington, R. Saltus, B. Schreckenberger, E. Thébault, F.
511   Caratori Tontini, 2009. "EMAG2: A 2-arc min resolution Earth Magnetic Anomaly Grid
512   compiled from satellite, airborne, and marine magnetic measurements," Geochemistry,
513   Geophysics, Geosystems, Q08005, v. 10, doi: 10.1029/2009GC002471, ISSN: 1525-2027.

514   Mayhew, M.A., 1982. An equivalent layer magnetization model for the United States derived
515   from satellite magnetic anomalies. J. Geophys. Res., 87, 4837-4845.

516   NOAA, 2005, http://www.ngdc.noaa.gov/geomag/WMM/.

517   Pawlowski, R.S., 1995. Preferential continuation for potential-field anomaly enhancement.
518   Geophysics, 60, 390-398.

519   Ravat, D., Whaler, K.A., Pilkington, M., Sabaka, T., Purucker, M., 2002. Compatibility of high-
520   altitude aeromagnetic and satellite-altitude magnetic anomalies over Canada. Geophysics,
521   67(2), 546-554.

522   Sabaka, T. J., N. Olsen, M. Purucker, 2004, Extending comprehensive models of the Earth's
523   magnetic field with Ørsted and CHAMP data, Geophys. J. Int., 159, 521–547.

524   Schnetzler, C.C., 1985. An estimation of continental crust magnetization and susceptibility from
525   Magsat data for the conterminous United States. J. Geophys. Res., 90, 2617-2620.

526   Strang van Hees, G., 1990. Stokes formula using Fast Fourier Techniques. Manu. Geod., 15, 235-
527   239.

528   Stroud, A. H., Secrest, D. 1966. Gaussian Quadrature Formulas. Prentice-Hall.

529   Thébault, E., Schott, J.J., Mandea, M., 2006. Revised spherical cap harmonic analysis: validation
530   and properties. J. Geophys. Res., 111, B01102, doi:10.1029/2005JB001269.

531   Thébault E., Gaya-Piqué L., 2008. Applied comparisons between SCHA and R-SCHA regional
532   modeling techniques. Geochem. Geophys. Geosys, 9, doi:10.1029/2008GC001953.

533   Verhoef, J., Roest, W.R., Macnab, R., Arkani-Hamed, J., Members of the Project Team, 1996.
534   Magnetic anomalies of the Arctic and North Atlantic Oceans and adjacent land areas; GSC
535   Open File 3125, Parts a and b (CD_ROM and project report); Geological Survey of Canada,
536   Dartmouth, NS.

537   von Frese R.R.B., Hinze, W.J., Braile, L.W., 1981. Spherical earth gravity and magnetic
538   anomaly analysis by equivalent point source inversion. Earth Planet. Sci. Lett. 53, 69-83.

539   von Frese, R.R.B, Ravat, D.N., Hinze, W.J., McGue, C.A., 1988. Improved inversion of
540   geopotential field anomalies for lithospheric investigations, Geophysics., 53, 375-385.

541   von Frese, R.R.B, Kim, H.R., Tan, L., Kim, J.W., Taylor, P.T., Purucker, M.E., Alsdorf, D.E.,
542   Raymond, C.A., 1999. Satellite magnetic anomalies of the Antarctic crust. Annali di
543   Geofisica, 42, 309-326.

544   von Frese, R.R.B., H.R. Kim, 2003. "Satellite magnetic anomalies for lithospheric exploration,"
545   in: P. Stauning, H. Lühr, P. Ultré-Guérard, J. LaBrecque, M. Purucker, F. Primdahl, J.L.
546   Jørgensen, F. Christiansen, P. Høeg, and K.B. Lauritsen (Ed.s), ØIST-4 Proceedings (4th
547   Ørsted International Science Team Conference), 115-118, Narayana Press, Copenhagen.

548   von Frese, R.R.B., Kim, H.R., Taylor, P.T., Asgharzadeh, M.F., 2005. Reliability of Champ
549   anomaly continuation. in: C. Reigber, H. Lühr, P. Schwintzer, J. Wickert (Eds.), Earth
550   Observation with CHAMP Results from Three Years in Orbit, Springer Verlag, Heidelberg,
551   287-292.

552   von Frese, R.R.B., A.V. Golynsky, H.R. Kim, L. Gaya-Piqué, E. Thébault, M. Chiappini, M.
553   Ghidella, A. Grunow, and the ADMAP Working Group, 2008, "The next generation
554   Antarctic digital magnetic anomaly map," in: Cooper, A.K., and C.R. Raymond (Eds.),
555   Proceedings of the 10th ISAES, USGS Open-File Rept. 2007-1047, doi:
556   10.3133/of2007.srp163.
557

588   fields, (C) by single EPS inversion with the 10-km field, and (D) by single EPS inversion

589   with 400-km field.

590

591   **Figure 5**. Comparison between the modeled and estimated (A) gravity (mGal) and (B) magnetic

592   fields (nT) in **Figure 3** and **Figure 4**, respectively: (upper) correlation coefficient,

593   (middle) root-mean-square (RMS) difference, and (lower) Log (RMS).

594

595   **Figure 6.** Estimating near-surface magnetic effects to fill in regional gaps in the ADMAP

596   airborne and marine anomaly survey coverage (Kim et al., 2004). (A) ADMAP near-

597   surface magnetic anomalies for the West Antarctic Peninsula and surrounding marine

598   areas at 5 km altitude. (B) **Map A** low-pass filtered for 400-km and longer wavelengths

599   with simulated gap outlined in white. (C) Simulated Magsat anomalies at 400 km altitude

600   from a crustal prism model of **Map B** evaluated to 3-nT accuracy. (D) Near-surface

601   magnetic anomaly estimates at 5 km altitude with the coverage gap filled in using the

602   simulated Magsat in **Map C**. (E) Simulated CHAMP anomalies at 350 km altitude

603   evaluated at 0.3-nT accuracy. (F) Near-surface magnetic anomaly estimates at 5 km

604   altitude with the coverage gap filled in using the simulated CHAMP data in **Map E**. (G)

605   Simulated Ørsted anomalies at 700 km altitude evaluated at 0.3-nT accuracy. (H) Near-

606   surface magnetic anomaly estimates with the coverage gap filled in using the simulated

607   Ørsted data in **Map G**.

608

609   **Figure 7**. Comparisons of magnetic anomaly gap predictions with a recently surveyed portion of

610   the regional gap located east of Coats Land and the Shackleton Range in Antarctica (Kim

611   et al., 2007). (A) Recently surveyed aeromagnetic anomalies within the red-bordered

612   rectangular area and (B) their 200-km and longer low-pass filtered components compare

613   well with (C) the gap predictions over the survey area obtained using joint CHAMP and

614   Ørsted data and the earlier aeromagnetic anomalies. The gap predictions from (D)

615   minimum curvature and (E) the spherical harmonic geomagnetic field model MF4 (Maus

616   and Rother, 2005) are also shown. The correlation coefficients between the regional

617   survey components in Map B and the predictions in **Map C**, **Map D**, and **Map E** are

618   0.45, -0.5, and -0.18, respectively.

619

620   **Figure 8.** Gravity anomalies calculated at 0 km (A), 16 km (B), and 20 km (C) from prism

621   models. **Map B** gives the differentially continued anomalies at 16 km from the multi-

622   altitude FT using the anomalies from **Map A** and **Map C**. **Map B** gives the related

623   anomaly differences (B - D) with the (minimum, maximum), mean, and standard

624   deviation values listed along the bottom. **Map F** and **Map G** were calculated by

625   conventional single-surface Fourier transform as the downward continuation of **Map C**

626   and upward continuation of **Map A**, respectively. Their anomaly differences relative to

627   the modeled effects at 16 km in **Map B** are given in **Maps H** and **Map I**, respectively.

628

629   **Figure 9.** (A) Aeromagnetic anomalies reduced-to-pole for Southern Greenland and surrounding

630   marine areas at 20 km altitude (Verhoef et al., 1996) and conventionally upward

631   continued to (B) 50 km, (C) 250 km, (D) 300 km, and (E) 350 km. (F) CHAMP based

632   MF6 model estimates at 350 km (Kim et al., 2010) that were combined with the anomaly

633   data in **Map A** for the dual-surface FT continuations at (G) 300 km, (H) 250 km, and (I)

634   50 km. Selected correlation coefficients between the maps are CC(E,F) = 0.16, CC(D,G)

635   = 0.61, CC(C,H) = 0.88, and CC(B,I) = 0.99.

636

637   **Figure 10.** Spherical cap harmonic analysis (SCHA) model of joint gravity anomalies at 20

638   km (a) and 0 km (c) altitudes evaluated at the intermediate altitude of 10 km (b).

639

640   **Figure 11.** Spherical cap harmonic analysis (SCHA) model of radial geomagnetic field

641   components   evaluated   from   global   KOMPSAT-1   three-axis   magnetometer

642   measurements during December 1999 at 685 km altitude (a) and SCHA model

643   estimates at the 20 km altitude of a U2 reconnaissance survey (b) and at the Earth

644   surface (d) (adapted from Kim et al., 2007).

Table 1. Performance statistics for using minimum curvature (MC) and Magsat (**Figure 3(B)**), Ørsted (**Figure 3(D)**), and CHAMP (**Figure 3(F)**) magnetic anomalies to fill a simulated gap in aeromagnetic anomaly coverage. The prediction statistics include the root-mean-square (RMS) difference, the correlation coefficient (CC), and related noise (N) levels. In the right four columns, the upper triangular portion gives the relative noise reductions for the gap predictions from the various constraints.

Constraint	RMS	CC	N	MC	Magsat	Ørsted	CHAMP
MC	108.7 nT	0.34	72%	0	44%	83%	94%
Magsat	98.5 nT	0.51	40%		0	70%	90%
Ørsted	74.5 nT	0.81	12%			0	67%
CHAMP	32.1 nT	0.93	4%				0

Table 2. Statistics of synthetic gravity data at 20, 10, and 0 km and correlation coefficients shown in **Figure 9** (unit: mGal).

	Min	Max	Standard Deviation	Correlation Coefficient		
				at 20 km	at 10 km	at 0 km
at 20 km	- 284.87	250.47	65.01	-	0.998	0.991
at 10 km	- 335.83	280.13	69.60	0.998	-	0.997
at 0 km	- 409.66	319.27	75.27	0.991	0.997	-

Table 3. Statistics and correlation coefficients of radial component of KOMPSAT-1 measurements estimated at satellite (685 km), U2 (20 km), and Earth surface (0 km) as shown in **Figure10** (unit: nT).

	Min	Max	Standard Deviation	Correlation Coefficient		
				at 685 km	at 20 km	at 0 km
at 685 km	- 55378.50	- 13201.80	8821.38	-	0.991	0.990
at 20 km	- 70959.30	- 22931.40	10743.58	0.991	-	1.0
at 0 km	- 71515.10	- 23270.30	10813.16	0.990	1.0	-
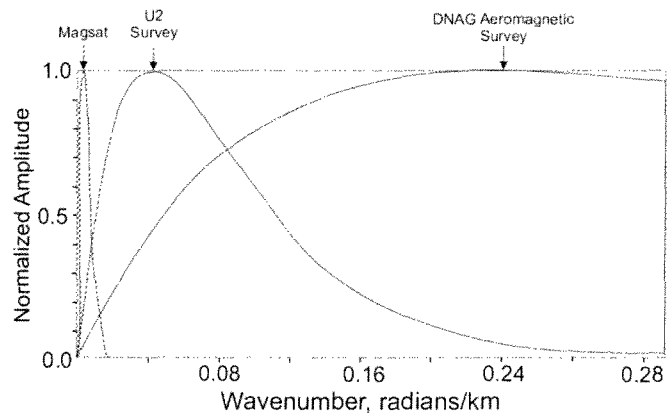
Figure 1. Normalized amplitude spectra from geomagnetic surveys at typical satellite (400 km), U2 (20km), and airborne (1 km) altitudes (adapted from Hildenbrand et al., 1996).
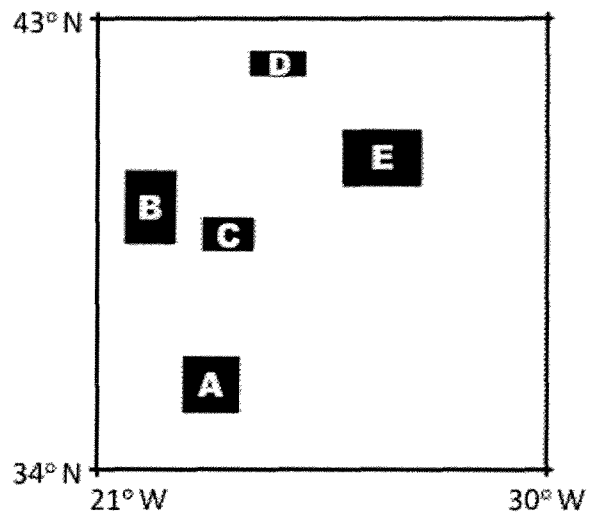
Figure 2. Location of the 5 crustal prisms. All prisms were 25 km thick with tops at 5 km below sea level and located in Balkan region between 34° - 43° N and 21° - 30° W.
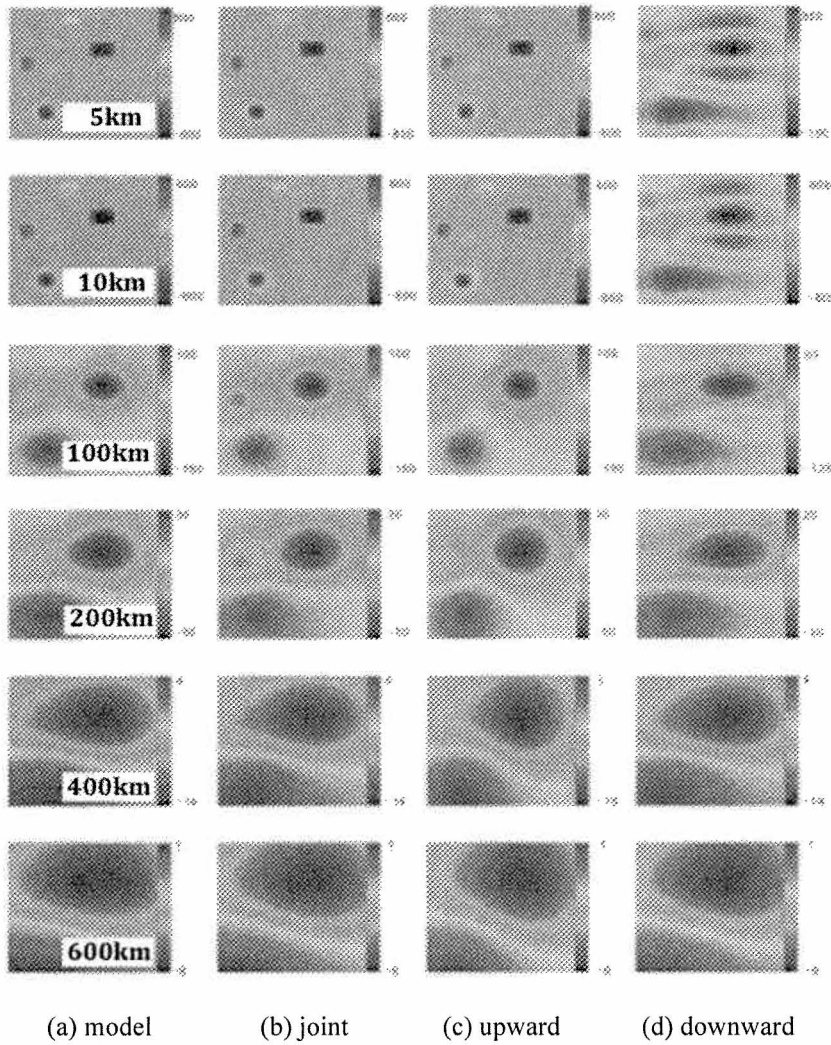
Figure 3. Gravity effects (mGal) from five prisms in the spherical coordinates modeled (A) directly from the GLQ integration, (B) by joint EPS inversion of the 10 km and 400 km fields, (C) by single EPS inversion with the 10 km field, and (D) by single EPS inversion with 400 km field.

(a) model   (b) joint   (c) upward   (d) downward
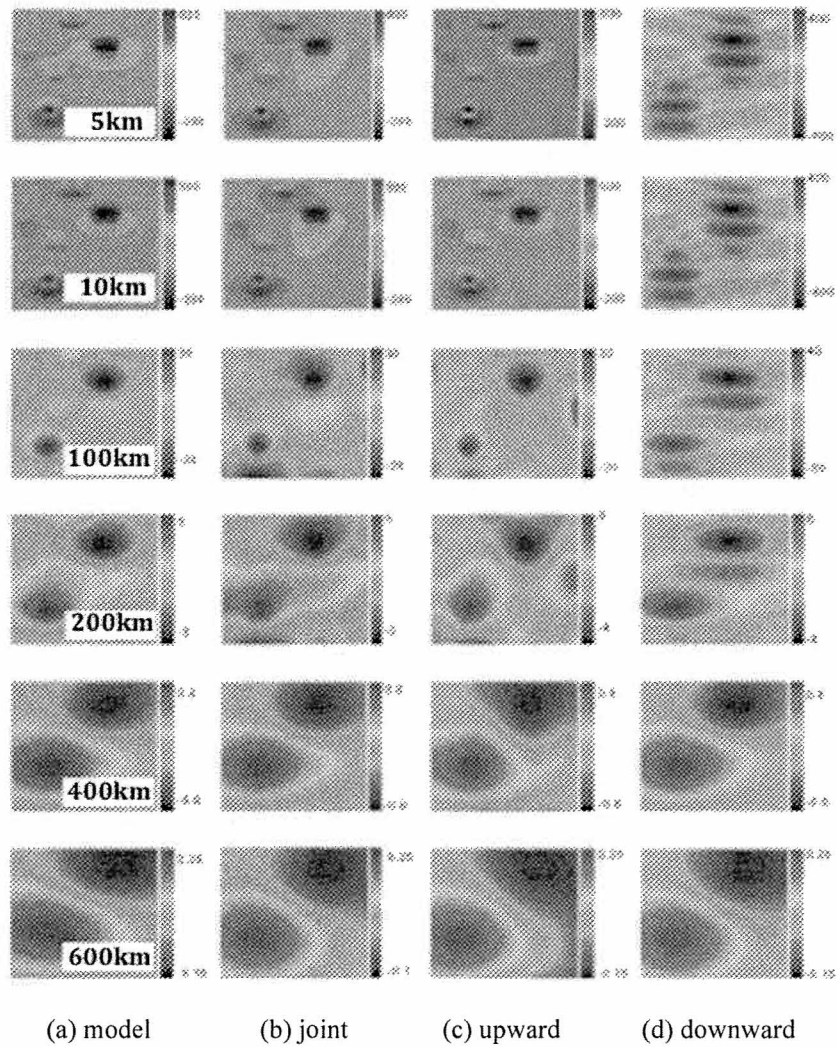
Figure 4. Magnetic effects (nT) from five prisms in the spherical coordinates modeled (A) directly from the GLQ integration, (B) by joint EPS inversion of the 10-km and 400-km fields, (C) by single EPS inversion with the 10-km field, and (D) by single EPS inversion with 400-km field.

A) Gravity Anomalies   (B) Magnetic Anomalies
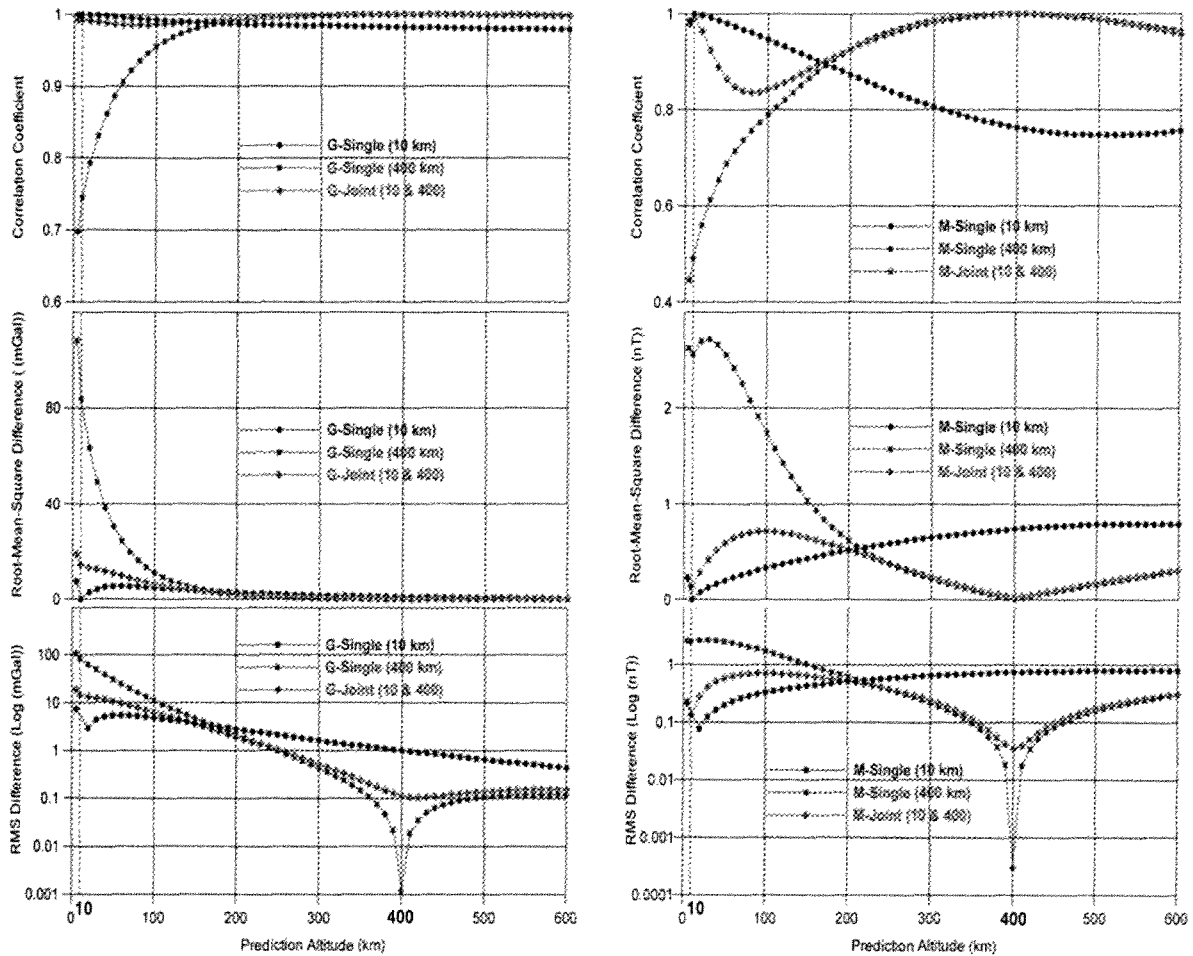
Figure 5. Comparison between the modeled and estimated (A) gravity (mGal) and (B) magnetic fields (nT) in **Figure 3** and **Figure 4**, respectively: (upper) correlation coefficient, (middle) root-mean-square (RMS) difference, and (lower) Log (RMS).
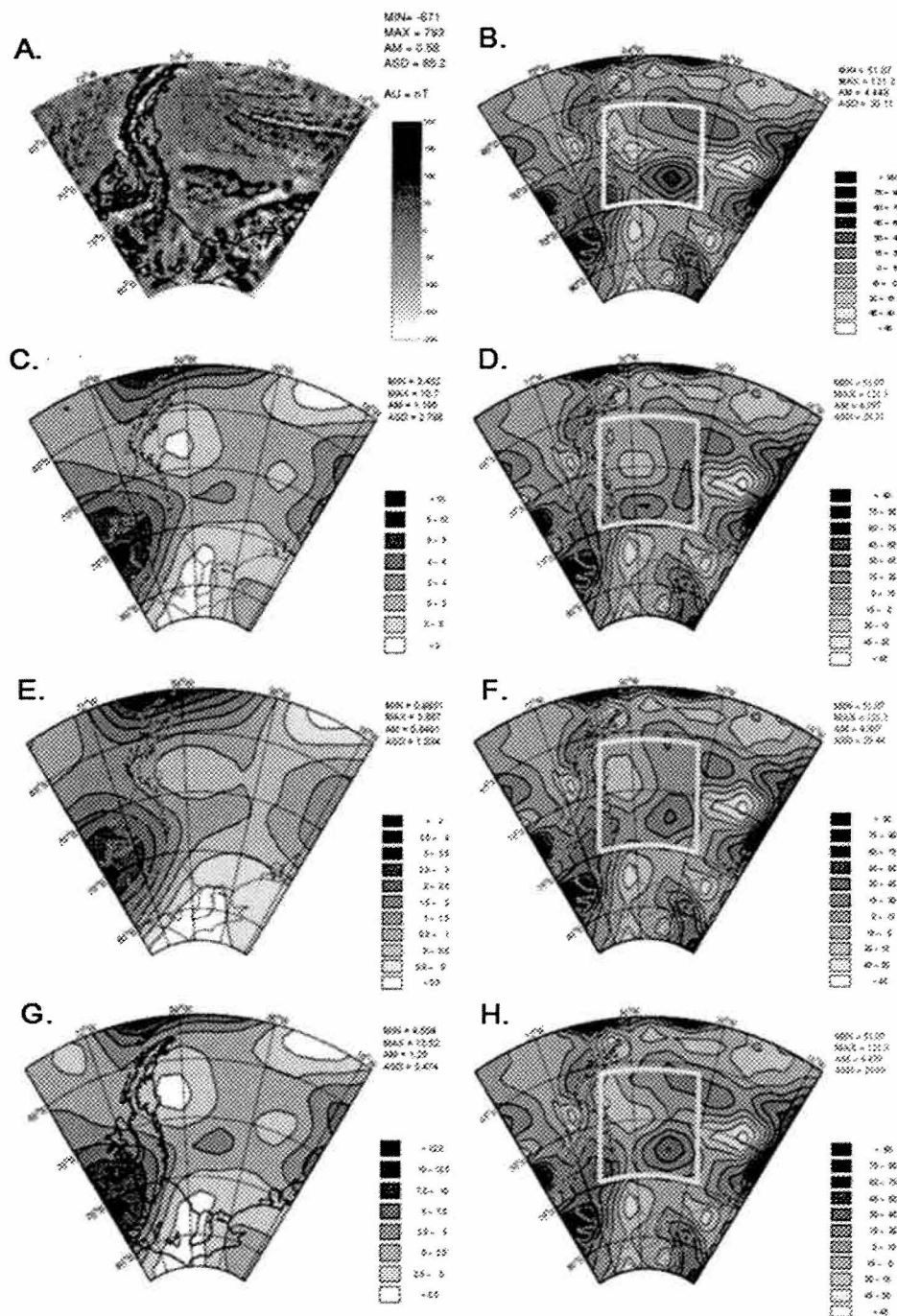
Figure 6. Estimating near-surface magnetic effects to fill in regional gaps in the ADMAP airborne and marine anomaly survey coverage (Kim et al., 2004). (A) ADMAP near-surface magnetic anomalies for

the West Antarctic Peninsula and surrounding marine areas at 5 km altitude. (B) **Map A** low-pass filtered for 400-km and longer wavelengths with simulated gap outlined in white. (C) Simulated Magsat anomalies at 400 km altitude from a crustal prism model of **Map B** evaluated to 3-nT accuracy. (D) Near-surface magnetic anomaly estimates at 5 km altitude with the coverage gap filled in using the simulated Magsat in **Map C**. (E) Simulated CHAMP anomalies at 350 km altitude evaluated at 0.3-nT accuracy. (F) Near-surface magnetic anomaly estimates at 5 km altitude with the coverage gap filled in using the simulated CHAMP data in **Map E**. (G) Simulated Ørsted anomalies at 700 km altitude evaluated at 0.3-nT accuracy. (H) Near-surface magnetic anomaly estimates with the coverage gap filled in using the simulated Ørsted data in **Map G**.
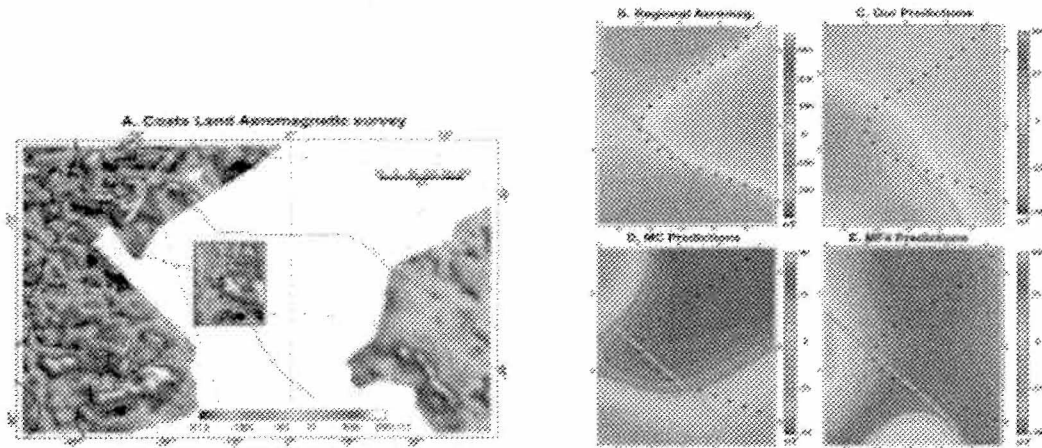
Figure 7. Comparisons of magnetic anomaly gap predictions with a recently surveyed portion of the regional gap located east of Coats Land and the Shackleton Range in Antarctica (Kim et al., 2007). (A) Recently surveyed aeromagnetic anomalies within the red-bordered rectangular area and (B) their 200-km and longer low-pass filtered components compare well with (C) the gap predictions over the survey area obtained using joint CHAMP and Ørsted data and the earlier aeromagnetic anomalies. The gap predictions from (D) minimum curvature and (E) the spherical harmonic geomagnetic field model MF4 (Maus and Rother, 2005) are also shown.   The correlation coefficients between the regional survey components in Map B and the predictions in **Map C**, **Map D**, and **Map E** are 0.45, -0.5, and -0.18, respectively.
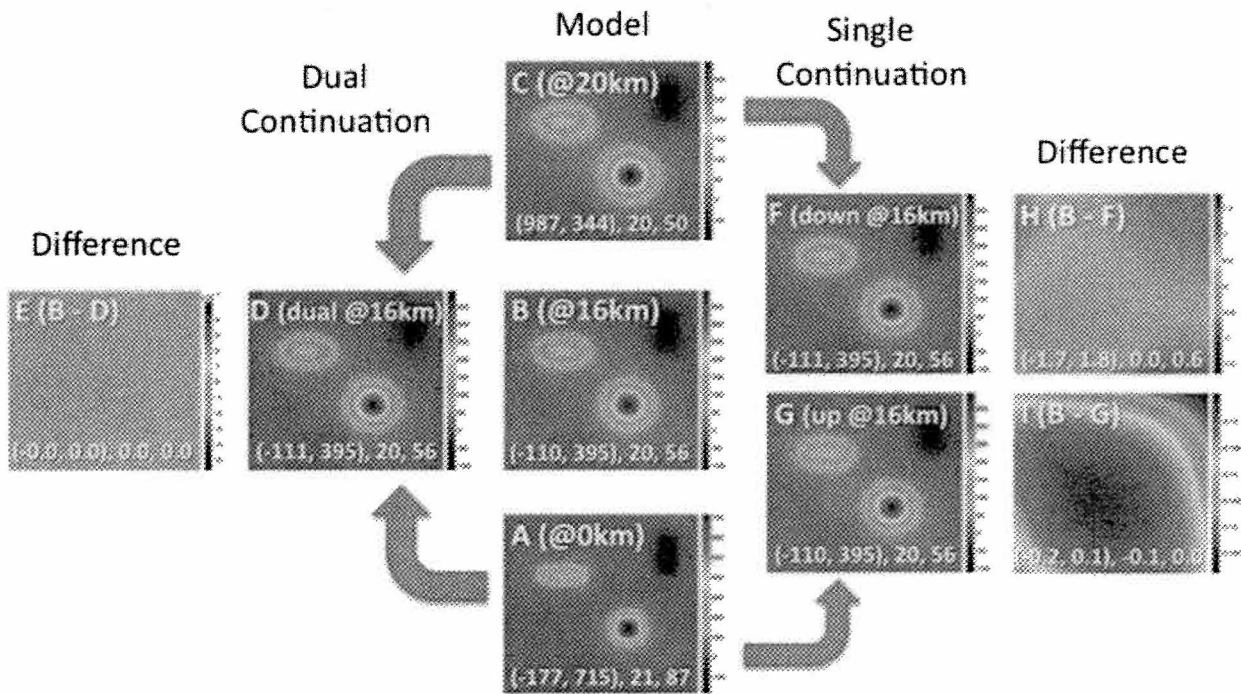
Figure 8. Gravity anomalies calculated at 0 km (A), 16 km (B), and 20 km (C) from prism models. **Map B** gives the differentially continued anomalies at 16 km from the multi-altitude FT using the anomalies from **Map A** and **Map C**. **Map B** gives the related anomaly differences (B - D) with the (minimum, maximum), mean, and standard deviation values listed along the bottom. **Map F** and **Map G** were calculated by conventional single-surface Fourier transform as the downward continuation of **Map C** and upward continuation of **Map A**, respectively. Their anomaly differences relative to the modeled effects at 16 km in **Map B** are given in **Maps H** and **Map I**, respectively.
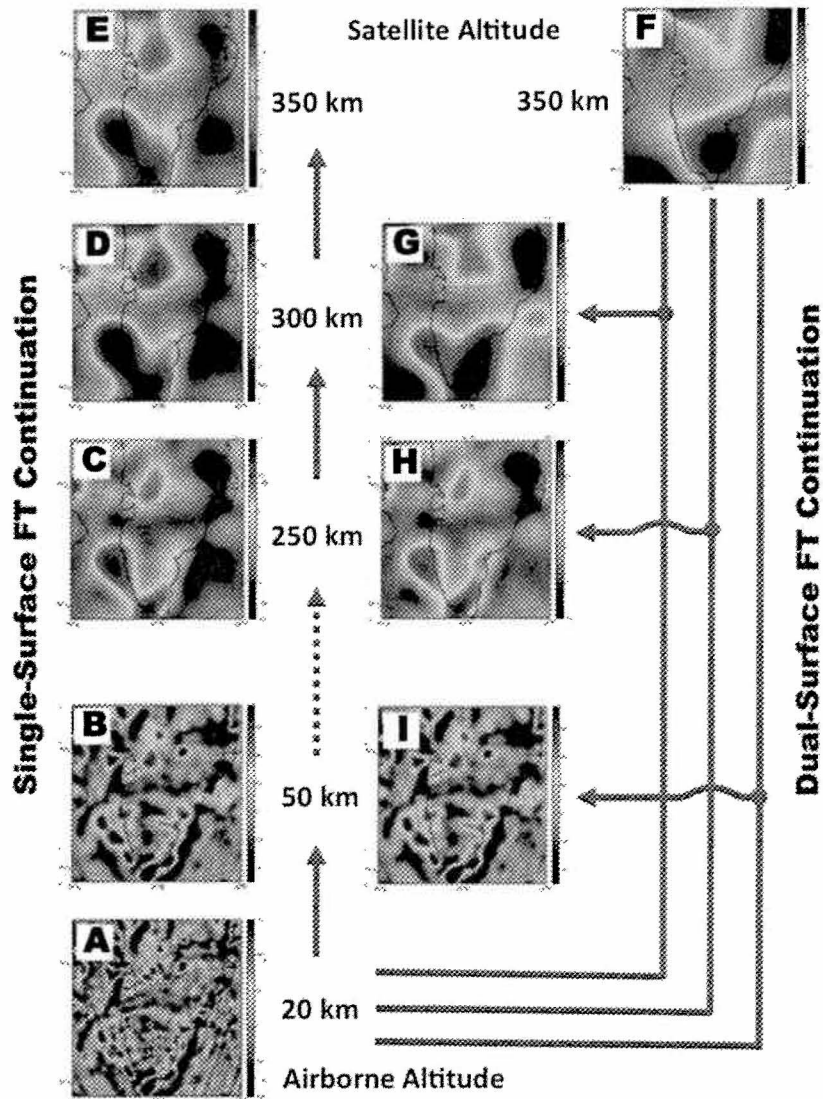
Figure 9. (A) Aeromagnetic anomalies reduced-to-pole for Southern Greenland and surrounding marine areas at 20 km altitude (Verhoef et al., 1996) and conventionally upward continued to (B) 50 km, (C) 250 km, (D) 300 km, and (E) 350 km. (F) CHAMP based MF6 model estimates at 350 km (Kim et al., 2010) that were combined with the anomaly data in **Map A** for the dual-surface FT continuations at (G) 300 km, (H) 250 km, and (I) 50 km. Selected correlation coefficients between the maps are CC(E,F) = 0.16, CC(D,G) = 0.61, CC(C,H) = 0.88, and CC(B,I) = 0.99.
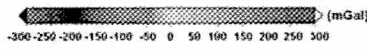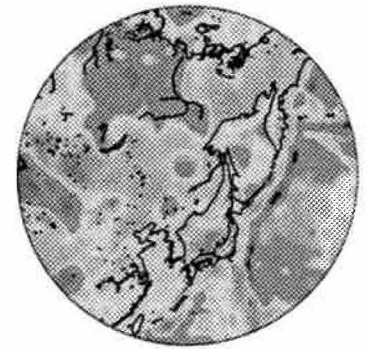
(a) 20 Km
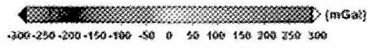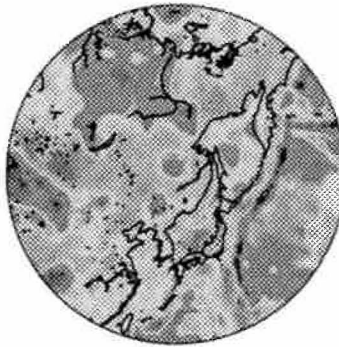
(b) 10 km
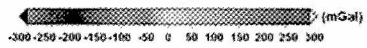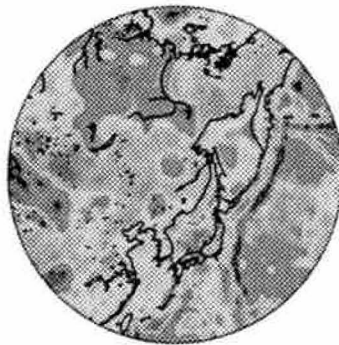
(c) 0 km

Figure 10. Spherical cap harmonic analysis (SCHA) model of joint gravity anomalies at 20 km (a) and 0 km (c) altitudes evaluated at the intermediate altitude of 10 km (b).

RADIAL: [AR=(-46044,44571)   AM=3408   ASD=29085   AU=nT]
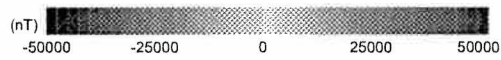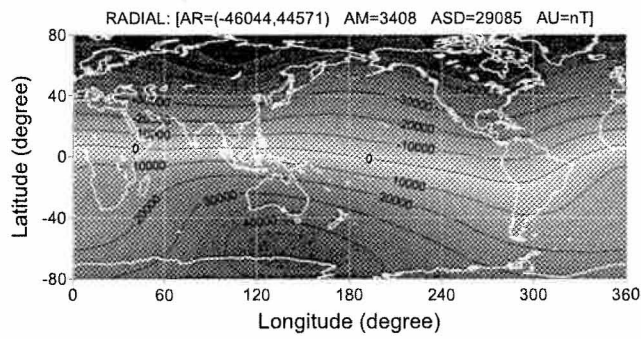
(a) Global KOMPSAT-1 (685 Km)
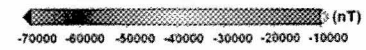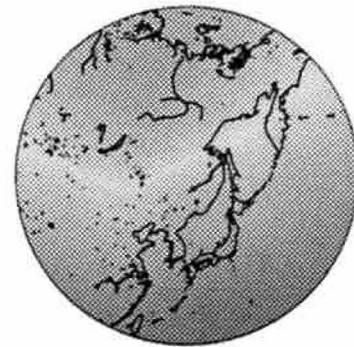
(b) Satellite (685 Km)
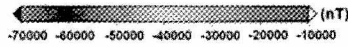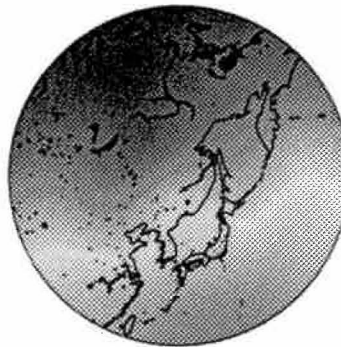
(c) U2 (20 Km)
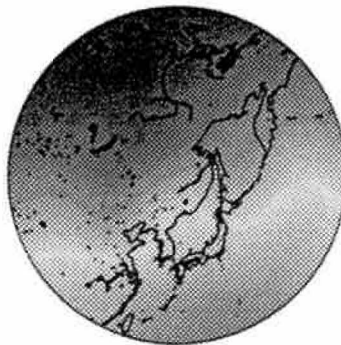
(d) Earth Surface (0 Km)

Figure 11. Spherical cap harmonic analysis (SCHA) model of radial geomagnetic field components evaluated from global KOMPSAT-1 three-axis magnetometer measurements

during December 1999 at 685 km altitude (a) and SCHA model estimates at the 20 km altitude of a U2 reconnaissance survey (b) and at the Earth surface (d) (adapted from Kim et al., 2007).